POM-incorporated ZnIn$_2$S$_4$ Z-scheme dual-functional photocatalysts for cooperative benzyl alcohol oxidation and H$_2$ evolution in aqueous solution

Fangshu Xing [a],[1], Renyou Zeng [a],[1], Chuchu Cheng [a], Qiuwen Liu [b], Caijin Huang [a],[*]

[a] *State Key Laboratory of Photocatalysis on Energy and Environment, College of Chemistry, Fuzhou University, Fuzhou 350108, PR China*
[b] *Ganjiang Innovation Academy, Chinese Academy of Sciences, Ganzhou, Jiangxi 341000, PR China*

ARTICLE INFO

ABSTRACT

Efficient aromatic alcohol oxidation with simultaneous H$_2$ evolution under aqueous conditions is achieved in a polyoxometalate (POM)-incorporated ZnIn$_2$S$_4$ dual-functional photocatalytic system. The synergy between HPM and ZIS contributes to the formation of a Z-type heterojunction structure and thus enhances redox capacity. Moreover, the sub-nanometer size of POM clusters endows molecular-level interfacial contact, which acts as an "electron bridge" ensuring faster interfacial charge transfer kinetics. Therefore, an impressive nearly 100% yield of benzaldehyde and 10.6 mmol·g^{-1}·h^{-1} H$_2$-evolution rate are observed for POM/ZIS nanocomposites even under an anaerobic atmosphere with water as the solvent. This is the first application of POM-based materials in the anaerobic oxidation of benzyl alcohol with concomitant H$_2$ production. This study expands the possibilities for designing multifunctional POM-based photocatalysts for economic and ecological photoredox applications.

1. Introduction

The utilization and conversion of solar energy into chemical fuels via artificial photosynthesis promotes the construction of a green, low-carbon, and sustainable energy system [1–4]. Compared with traditional organic syntheses that usually proceed under elevated temperature or pressure, photocatalysis provides an alternative way to achieve uphill reactions under mild conditions by virtue of photogenerated charges (i.e., electrons and holes) in high-energy excited states [5–8]. In the field of C—H bond activation in organic chemistry, the selective oxidation of aromatic alcohols to carbonyl compounds (e.g., aromatic aldehydes, ketones, and acids) remains one of the vital transformations because the carbonyl products possess widespread applications in fine chemical and pharmaceutical industries as versatile structural building blocks [9–13]. In this regard, many state-of-the-art efforts focus on the photoconversion of aromatic alcohols under aerobic conditions, wherein molecular oxygen (O$_2$) is usually employed as an electron acceptor and oxidant. The resulting reactive oxygen species (e.g., $^\bullet$O$_2^-$ [14,15], ^{1}O$_2$ [16,17]) are helpful to promote alcohol oxidation rates. However, this aerobic strategy suffers from drawbacks in practical applications due to the waste of photogenerated electrons.

Compared with the monoaromatic alcohol oxidation system above, a dual functional photocatalytic strategy provides an innovative way to merge alcohol oxidation with a meaningful reduction reaction [18,19]. The corresponding overall photoredox process avoids using additional sacrificial and oxidant agents and makes full use of photoexcited electron–hole pairs, which is in line with economic and ecological prospects. Furthermore, green hydrogen production from renewable energy has emerged as a sustainable process for a low-carbon future [2,4]. Therefore, developing an efficient dual-functional photocatalytic system for cooperative H$_2$ evolution and selective aromatic alcohol oxidation is promising in the co-production of clean fuels and value-added chemicals [18,19]. In this typical attempt, many dual-functional systems experience unsatisfactory aromatic alcohol conversion performance without oxidant assistance. Additionally, organic solvents (e.g., benzotrifluoride, acetonitrile, and hexane) are often used as reaction media to improve the solubility of alcohol substrates and enhance the yield (Tables S4 and S5). While avoiding costly and potentially harmful organic solvents would be ideal, achieving highly selective aromatic alcohol transformation in aqueous solution remains challenging. Consequently, it is highly desirable to design a precise dual-functional photocatalyst for matched photocatalytic aromatic alcohol oxidation and H$_2$ production under environmentally friendly aqueous conditions.

Polyoxometalates (POMs) are a family of unique inorganic

---

complexes constructed by countercations and metal-oxygen anionic clusters from high-valence early transition metals (e.g., V^{5+}, Nb^{5+}, Ta^{5+}, Mo^{6+}, and W^{6+}) [20,21]. The atomically well-defined structure, tunable acid–base properties, and inherent thermal, hydrolytic, and oxidative stability make POMs an emerging class of catalysts [22]. POMs are often recognized as electron reservoirs because unoccupied D-orbitals in high-valence metal centers have a solid capacity to undergo reversible multielectron transformations [22]. This unique high redox ability makes POMs active in various oxidation reactions, such as oxidation of alkenes, alkanes, arenes, alcohols, and C-C coupling [23–25]. Moreover, like semiconductors, POMs can absorb light and produce photo-generated electrons and holes owing to the oxygen-to-metal charge transfer (HOMO–LUMO transition) [26,27]. Thus, many photocatalytic oxidation reactions (e.g., oxidation of aromatic alcohol [28], styrene [29], benzene [30], and toluene [31]) proceed readily in the presence of POMs, overcoming the harsh conditions necessary for thermocatalysis [24,26]. Nevertheless, additional oxidants such as O_2 [24,32,33] (or O_2 from air [34,35]) or H_2O_2 [36] are always needed in these POM-mediated oxidation applications to oxidize excited-state POMs to the ground state or assist substrate oxidation. In addition, most POMs are highly soluble in reaction solvents and thus suffer from difficult recovery and recycling from a homogeneous system. Meanwhile, the low LUMO energy level of POMs restricts their application in reduction reactions [37]. Inspired by natural photosynthesis [38], rational design of a heterogeneous artificial Z-scheme photocatalytic system is an exciting challenge that can solve the issues described above, as it could not only inherit the remarkable oxidation advantage of POMs and explore more economical reduction reactions but also immobilize POM clusters.

Recently, molybdenum (Mo)-based heteropolyoxometalates have been extensively utilized in oxidation reactions as low-cost and environmentally benign catalysts [22]. Moreover, unsaturated Mo sites have been reported as active centers favoring the activation and cleavage of the C–H bond in benzyl alcohol (BA) [39]. Hence, stable phosphomolybdic acid (HPM) clusters with solid visible absorption [40] are ideal oxidation candidates to build dual-functional–Z-scheme photocatalytic systems for coupled BA oxidation and H_2 release. Notably, as sub-nanometer building blocks, POM clusters allow construction of exquisite nanocomposites with molecular-level interfacial contact, which is of importance to promote the transfer and separation of photogenerated charge carriers near the interface and enhance photocatalytic performance. Meanwhile, ultrathin two-dimensional (2D) materials are known for their rich specific surface exposing active sites and minimizing diffusion distances for electrons and holes [3]. In this regard, a 2D $ZnIn_2S_4$ (ZIS) nanosheet is chosen as a reduction component to couple with the HPM cluster [41]. The precise control of composition and structure may give us more insights into the structure-activity relationship in this rationally designed dual-functional photocatalytic system.

Herein, we present cooperative photocatalysis for selective BA oxidation with H_2 production in an environmentally benign aqueous medium by designing Z-scheme photocatalysts of HPM cluster-incorporated ZIS nanosheets (HPM/ZIS). This dual-functional photocatalytic system represents the first application of POM-based materials in anaerobic oxidation of BA integrated with H_2 evolution, which avoids the use of additional oxidants and realizes the simultaneous utilization of electron–hole pairs. The sub-nanosized POM building blocks provide molecular-level interfacial contact in the HPM/ZIS nanocomposites via a secondary-component incorporation strategy, ensuring faster charge transfer at the interface. Meanwhile, the expected Z-scheme charge transfer path regulated by a built-in electric field was well corroborated by XPS and EPR experiments. Based on activity contrast experiments, two kinds of possible reaction pathways for photocatalytic dehydrogenation oxidation of BA are proposed to better understand the reaction mechanism.

2. Experimental section

2.1. Chemicals

All chemical reagents were of analytical grade and used as received without any further purification. Anhydrous zinc chloride ($ZnCl_2$) was obtained from Macklin. Indium nitrate hydrate ($InCl_3·4H_2O$), thio-acetamide (C_2H_5SN, TAA), carbon tetrachloride (CCl_4), anhydrous ethanol (C_2H_6O), and triethanolamine ($C_6H_{15}NO_3$, TEOA) were supplied by Sinopharm Chemical Reagent Co. Ltd. Phosphomolybdic acid ($H_3PMo_{12}O_{40}$, HPM), benzyl alcohol (C_7H_8O, PhCH$_2$OH, BA), benzaldehyde (C_7H_6O, PhCHO, BAD), 4-methylbenzyl alcohol ($C_8H_{10}O$), 4-methoxybenzyl alcohol ($C_8H_{10}O_2$), 4-chlorobenzyl alcohol (C_7H_7ClO), 4-bromobenzyl alcohol (C_7H_7BrO), 5,5-dimethyl-1-pyrroline N-oxide (DMPO), isopropanol (C_3H_8O, IPA), diphenylamine (Ph_2NH, DPA), N,N-dimethylformamide (C_3H_7NO, DMF) were purchased from Aladdin. Xinhang Gas Co. Ltd. provided argon gas (Ar) with 99.9% purity.

2.2. Materials synthesis

2.2.1. Synthesis of ZnIn$_2$S$_4$ nanoflowers
$ZnIn_2S_4$ (ZIS) nanoflowers were synthesized based on the procedure in our previous report [42,43].

2.2.2. Synthesis of HPM-incorporated ZnIn$_2$S$_4$ flower-like nanohybrids
First, a calculated amount of Keggin-type phosphomolybdic acid hydrates (HPM) was dissolved in ethanol (20 mL) followed by the addition of $ZnCl_2$ (0.136 g, 1 mmol) and $InCl_3·4H_2O$ (0.586 g, 2 mmol). After forming a homogeneous solution, TAA (0.3 g, 4 mmol) was added to the above system and stirred for 30 min. The resulting mixture was transferred to a 50 mL Teflon-lined autoclave, and then heated at 120 °C for 2 h. After washing the products with ethanol and water via centrifugation and then drying at 60 °C, HPM-incorporated ZIS nanohybrids (PAZ) were obtained. According to the nominal weight percentage (x%) of HPM to ZIS, the PAZ nanohybrids were labeled as PAZ-x (x = 0.05, 0.5, 1, 1.5, 2, and 3). Specifically, the corresponding HPM contents are 0.21, 2.11, 4.23, 6.35, and 12.69 mg (0.115, 1.156, 2.317, 3.479, and 6.952 µmol), respectively. The actual weight ratio of HPM to ZIS was measured by inductively coupled plasma−optical emission spectrometry (ICP−OES) (Table S3), and the experimentally determined weight ratio was close to the nominal weight percentage.

2.3. Characterizations

X-ray diffraction (XRD) patterns were collected on an X-ray diffractometer (Cu Kα irradiation, λ = 1.5406 Å, 40 kV, 40 mA, D8 Advance, Bruker). Fourier-transform infrared (FT–IR) spectra were obtained by a Thermo Nicolet IS50 spectrometer using the attenuated total reflectance (ATR) method. Morphology analyses were performed by field emission scanning electron microscopy (SEM, SU-8010, Hitachi) and transmission electron microscopy (TEM, FEI Talo F200S, Thermo Fisher Scientific) operating at a voltage of 200 kV. Chemical states were studied with an X-ray photoelectron spectrometer (XPS, ESCALAB 250Xi, Thermo Fisher Scientific) using monochromatic Al Kα as the X-ray source. The XPS spectra were calibrated with a peak position of 284.6 eV for C 1 s. Ultraviolet photoemission spectroscopy (UPS, ESCALAB 250Xi, Thermo Fisher Scientific) was performed to evaluate the energy band structure of HPM using the He I UPS spectrum from the excitation energy (21.22 eV). UV–Vis diffuse reflectance spectra (DRS) were recorded on a UV–Vis spectrophotometer (Cary 5000, Varian) with $BaSO_4$ as the reflectance standard. Nitrogen adsorption–desorption isotherms were collected on a physical adsorption instrument at 77 K (3020, Micromeritics). The specific surface area was calculated using the Brunauer−Emmett−Teller (BET) method. Pore size distribution was obtained by the BJH model. Atomic force microscopy (AFM) measurements (Dimension Icon, Bruker) were conducted to measure the thickness of the samples. Zeta

potential was measured by a Malvern zeta potential analyzer. The concentrations of molybdenum ions were detected by inductively coupled plasma−optical emission spectrometry (ICP−OES, ICPOES730, Agilent). Time-resolved transient photoluminescence decay (TR-PL) spectra were recorded on a HORIBA DeltaPro with a 350 nm laser. Steady-state photoluminescence (PL) spectra were obtained at an excitation wavelength of 280 nm (Fluorolog-3-TCSPC, HORIBA). Electron paramagnetic resonance (EPR) data were recorded at room temperature using a Bruker A300 spectrometer (microwave frequency of 9.86 GHz, modulation amplitude of 3 G, modulation frequency of 100 kHz, attenuator of 15 dB). Isotope-labeled products were analyzed by isotope ratio mass spectrometry (Delta V Plus, Thermo Fisher Scientific).

2.4. Photoelectrochemical measurements

All photoelectrochemical measurements were carried out in a standard three-electrode system on a Bio-Logic electrochemical workstation at room temperature. The reference and counter electrodes were the Ag/AgCl and Pt wires, respectively. The working electrode (thin sample film) was prepared by dropping 20 μL ink (mixture of 20 mg catalyst, 20 μL Nafion, and 0.5 mL DMF) onto fluorine-tin oxide (FTO) glass with an exposed circular area of 0.28 cm^2. The electrolyte for photocurrent, Mott–Schottky, and linear sweep voltammetry (LSV) tests was 0.5 M Na_2SO_4 solution. The photocurrent-time (I–t) curves were tested under visible-light irradiation at 0.2 V bias voltage. Mott–Schottky plots were taken at AC frequencies of 0.5, 1, and 1.5 kHz, respectively. The LSV measurements were carried out at a scan rate of 5 mV·s^{-1}. Electrochemical impedance spectra (EIS) were measured under open-circuit voltage with frequencies ranging from 10^{-2} to 10^5 Hz (AC amplitude of 10 mV). The electrolyte for the EIS test was a $K_3[Fe(CN)_6]/K_4[Fe(CN)_6]/KCl$ (10 mmol·L^{-1}/10 mmol·L^{-1}/0.5 mol·L^{-1}) mixed solution. The measured potential vs. Ag/AgCl was converted to the reversible hydrogen electrode (RHE) scale with the Nernst equation:

$$E_{RHE} = E_{Ag/AgCl} + 0.059 \times pH + E_{Ag/AgCl}^{\theta} \qquad (1)$$

where $E_{Ag/AgCl}^{\theta} = 0.197$ V at 25 °C.

2.5. Photocatalytic performance tests

2.5.1. Photocatalytic aerobic oxidation of benzyl alcohol coupled with hydrogen evolution

Photocatalytic benzyl alcohol oxidation integrated with H_2 evolution was performed in a homemade glass reactor with a quartz window and a double-walled jacket. The reaction temperature was kept at 25 °C by circulating water. The as-prepared photocatalyst (5 mg) was dispersed in 10 mL benzyl alcohol aqueous solution (0.02 mol L^{-1}) through ultrasonication. The reactor was purged with Ar gas for 10 min under stirring to remove air and then sealed. Subsequently, the reaction was carried out under irradiation ($\lambda > 420$ nm, 300 W Xe lamp) for 5 h. The produced H_2 was quantified by gas chromatography (GC, FULI 9750 , TCD detector, 5 A sieve column, Ar as carrier gas). After the reaction, the suspension was filtered through a 0.22 μm nylon syringe filter. The reaction solution was analyzed by high-performance liquid chromatography (HPLC, Waters 1525, Waters 2998 Photodiode Array Detector, C18 column). The conversion of benzyl alcohol (BA) and the selectivity for benzaldehyde (BAD) were calculated as follows:

$$\text{Conversion } (\%) = \frac{C_0 - C_{BA}}{C_0} \times 100\% \qquad (2)$$

$$\text{Selectivity } (\%) = \frac{C_{BAD}}{C_0 - C_{BA}} \times 100\% \qquad (3)$$

where C_0, C_{BA}, and C_{BAD} are the concentrations of initial benzyl alcohol, residual benzyl alcohol, and produced benzaldehyde, respectively.

The apparent quantum yield (AQY) for H_2 evolution was measured under the same photocatalytic reaction conditions but using light-emitting diodes (LEDs) as light sources. The incident wavelengths included 365, 420, 460, 520, and 650 nm. Moreover, the corresponding average light intensities were 10.86, 11.46, 13.75, 12.48, and 10.05 mW·cm^{-2}. The irradiation area was approximately 3.14 cm^2. The AQY was calculated as following equation:

$$\text{AQY} = \frac{N_e}{N_p} \times 100\% = \frac{2 \times \text{number of } H_2 \text{ moleculars}}{\text{numer of incident photons}} \times 100\%$$

$$= \frac{2 \times n_{H_2} \times N_A \times h \times c}{S \times P \times t \times \lambda} \times 100\% \qquad (4)$$

where N_e represents the total reactive electrons; N_p represents the total incident photons; n_{H_2} represents the moles of H_2; N_A is the Avogadro constant; h is the Planck constant; c is the lightspeed; S represents the irradiation area; P represents the average incident light intensity; t is the reaction time; and λ is the irradiation wavelength.

2.5.2. Substrate extension experiments

Photocatalytic conversion of different aromatic alcohols (R-PhCH$_2$OH, R = H, OCH$_3$, CH$_3$, Cl, and Br) coupled with H_2 production was also conducted under similar conditions except for the substitution of the reaction substrate.

2.5.3. Activity contrast experiments for photocatalysis mechanism

A range of active species and carrier trapping experiments were conducted to explore the reaction mechanism in the conversion of benzyl alcohol. Equivalent quenching agents (0.2 mmol), including carbon tetrachloride (CCl$_4$), triethanolamine (TEOA), isopropanol (IPA), 5,5-dimethyl-1-pyrroline N-oxide (DMPO), and diphenylamine (DPA), were utilized in the reaction of benzyl alcohol oxidation coupled with H_2 evolution. Typically, CCl$_4$ and TEOA consume electrons and holes, respectively. IPA is a scavenger for hydroxyl radicals ($^\bullet$OH). DPA can capture oxygen-centered radical species ($^\bullet$PhCH$_2$O) from benzyl alcohol (PhCH$_2$OH). Both carbon-centered radical species ($^\bullet$PhCHO$^-$) and oxygen-centered radical species ($^\bullet$PhCH$_2$O) from PhCH$_2$OH can be trapped by DMPO.

2.5.4. Stability experiments

After each cycle (5 h), the reaction mixture was filtered and washed with water, and then the recycled sample was employed for the continuous performance test.

3. Results and discussion

3.1. Structure, morphology, and composition analyses

A secondary-component incorporation strategy was adopted to induce intimate interfacial contact between ZIS and HPM clusters. In detail, HPM-incorporated ZIS nanohybrids (PAZ) were prepared via a facile one-pot solvothermal process using HPM as an additive (Fig. 1a). Because of their nanoscale size, HPM clusters can be assembled with ZIS crystal nuclei and embedded evenly into ZIS nanosheets. The X-ray diffraction (XRD) patterns of PAZ samples and ZIS (Fig. 1b) match well with the standard card of hexagonal ZnIn$_2$S$_4$ (JCPDS No. 65–2023). However, no characteristic peaks of HPM were observed, indicating that HPM clusters are well dispersed on ZIS [20]. Specifically, the diffraction peak at 21.26° assigned to the (006) plane for the PAZ samples shifts toward a lower angle, and the (004) diffraction peak at 14.19° disappears (Fig. 1c) as the mass ratio of HPM to ZIS is above 1%. The incorporation of HPM clusters presumably causes such slight lattice changes [44]. HPM with a Keggin structure consists of one central PO$_4$ tetrahedron surrounded by twelve MoO$_6$ octahedra as depicted in Fig. 1d (H$_3$PMo$_{12}$O$_{40}$, JCPDS No. 43–0316). The four characteristic infrared (IR) peaks of HPM located at 727, 866, 955, and 1058 cm^{-1} (Fig. S1) are
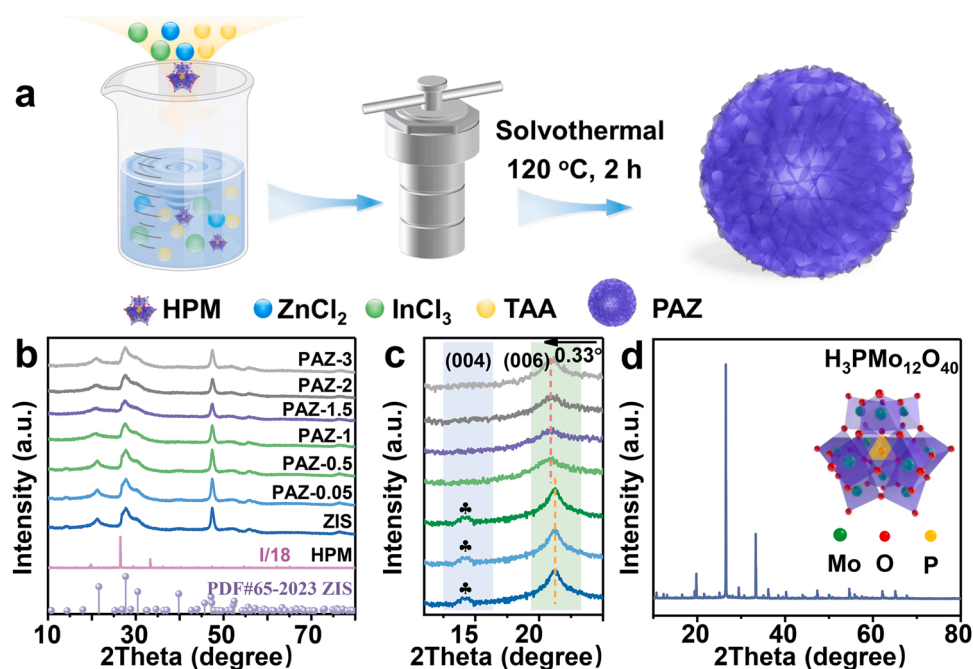
Fig. 1. (a) Schematic synthesis process of HPM-incorporated ZIS nanohybrids (PAZ). (b) XRD patterns of HPM, ZIS, and PAZ-x samples (x represents the mass ratio of HPM to ZIS). (c) Enlarged part from (b). (d) XRD pattern and Keggin structure of HPM.
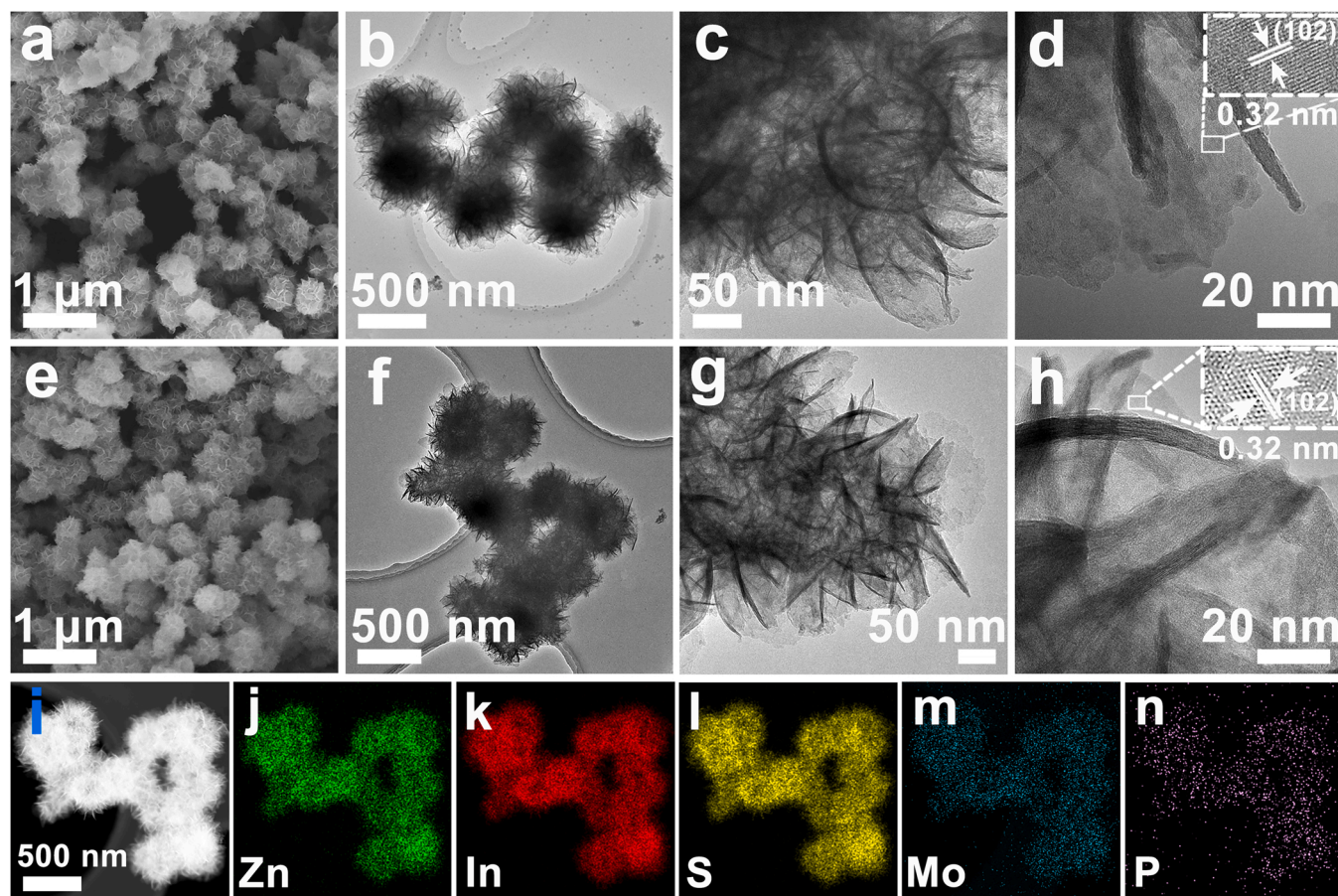
Fig. 2. (a) SEM, (b, c) TEM, and (d) HRTEM images of ZIS. (e) SEM, (f, g) TEM, and (h) HRTEM images of PAZ-1. (i) HAADF-STEM image of PAZ-1 and corresponding elemental mappings for (j) Zn, (k) In, (l) S, (m) Mo, and (n) P.

attributed to the vibrations of Mo–O_c–Mo (O_c: bridging atoms, corner-sharing), Mo–O_b–Mo (O_b: bridging atoms, edge-sharing), Mo=O_d (O_d: terminal O atoms), and P–O_a (O_a: central O atoms in PO_4 tetrahedron) bonds, respectively [30]. The above signals also present in the IR spectra of the PAZ-10 and PAZ-20 samples, whereas they are absent for the PAZ-x (x ≤ 3) samples due to the low content of HPM. Since pure ZIS has no IR response, the signals of PAZ samples located in green and pink regions belong to surface-adsorbed water and ethanol, respectively.

Scanning electron microscopy (SEM) and transmission electron microscopy (TEM) images show that both ZIS and PAZ-1 samples possess hierarchical nanoflower-like architecture composed of ultrathin nanosheets (Fig. 2). As depicted in AFM images (Fig. S2), the thickness of the nanosheets in ZIS and PAZ-1 is approximately 4.5 nm, corresponding to four $ZnIn_2S_4$ monolayers [45]. The HRTEM images of ZIS and PAZ-1 (Fig. 2d–h) present the characteristic spacing of 0.32 nm assigned to the (102) plane of ZIS, confirming that ZIS still undergoes the usual nucleation and growth processes in the presence of a few HPMs. The elemental mappings (Fig. 2j–n) of PAZ-1 further prove the existence and complete coverage of Zn, In, S, Mo, and P elements, giving direct evidence for the uniform insertion of HPM. This texture favors the well-defined heterointerface between HPM clusters and ZIS. The specific surface areas of PAZ-1 and ZIS are 130.4 and 89.6 $m^2 \cdot g^{-1}$, respectively (Fig. S3a). The increased surface area may expose more active sites. Moreover, ZIS and PAZ-1 show similar pore size distributions centered at 3.6 nm (Fig. S3b), allowing BA molecules to feasibly diffuse into the mesopores of ZIS and PAZ samples.

X-ray photoelectron spectroscopy (XPS) was conducted to probe the composition and chemical state information of the prepared samples. The survey spectra show that PAZ samples possess a similar abundance of Zn, In, and S elements to ZIS (Fig. 3a). For pure ZIS, the binding energies of Zn 2p (1021.9 and 1045.0 eV), In 3d (444.8 eV and 452.3 eV), and S 2p (161.7 and 162.9 eV) are attributed to Zn^{2+}, In^{3+}, and S^{2-} ions,

respectively [45]. Noticeably, the spectra of Zn 2p, In 3d, and S 2p in the PAZ-X (X = 1, 2, 3) samples consecutively shift to higher binding energies compared to pristine ZIS (Fig. 3b–d; Table S1). The decreased electron density in ZIS component suggests the interfacial electron transfer from ZIS to HPM in PAZ composites. Compared with the Mo^{6+} state (232.98 and 236.14 eV) in pristine HPM (Fig. S4a), the Mo^{4+} state (229.60 and 232.81 eV) [37] occurs in PAZ-3 (Fig. 3e), indicating the partial reduction of Mo^{6+}. Furthermore, the EPR tests show progressively strengthened paramagnetic responses of Mo^{5+} from PAZ-0.05 to PAZ-3 (Fig. 3f). It is known that high-valence state Mo^{6+} sites in HPM tend to undergo reversible multielectron transfer, and the electrons received by the $[PMo_{12}O_{40}]^{3-}$ unit are localized in the metal center so that some Mo^{6+} elements are reduced to lower valence states [24,46]. Therefore, the coexistence of reduced-state Mo species (Mo^{4+} and Mo^{5+}) in PAZ samples (Fig. 3e and f) fully verifies the flow of interfacial electrons from ZIS to HPM, which can be driven by the built-in electric field in HPM/ZIS heterojunctions.

3.2. Optical properties and band structure analyses

The light-harvesting capabilities of pure ZIS, HPM, and PAZ nanohybrids were evaluated through UV–Vis absorption spectra (Fig. 4a). ZIS exhibits an intense absorption in the visible light region below 500 nm. The intrinsic absorption of HPM is located below 550 nm with a steep absorption edge, which is attributed to ligand-to-metal charge transfer (LMCT) bands [26]. Additionally, pristine HPM displays a slight absorption tail centered at 760 nm because of the intervalence charge transfer (IVCT) from Mo^{5+} to Mo^{6+}. Mo^{5+} may come from a slight amount of Mo^{6+} being reduced by photogenerated electrons during the test [47]. After incorporation of HPM, the light response of PAZ samples distinctly strengthens in the visible light region compared to pure ZIS. Based on the Tauc plot (Fig. 4b), the bandgap energies of ZIS and HPM were calculated to be 2.73 and 2.47 eV, respectively. The flat potential
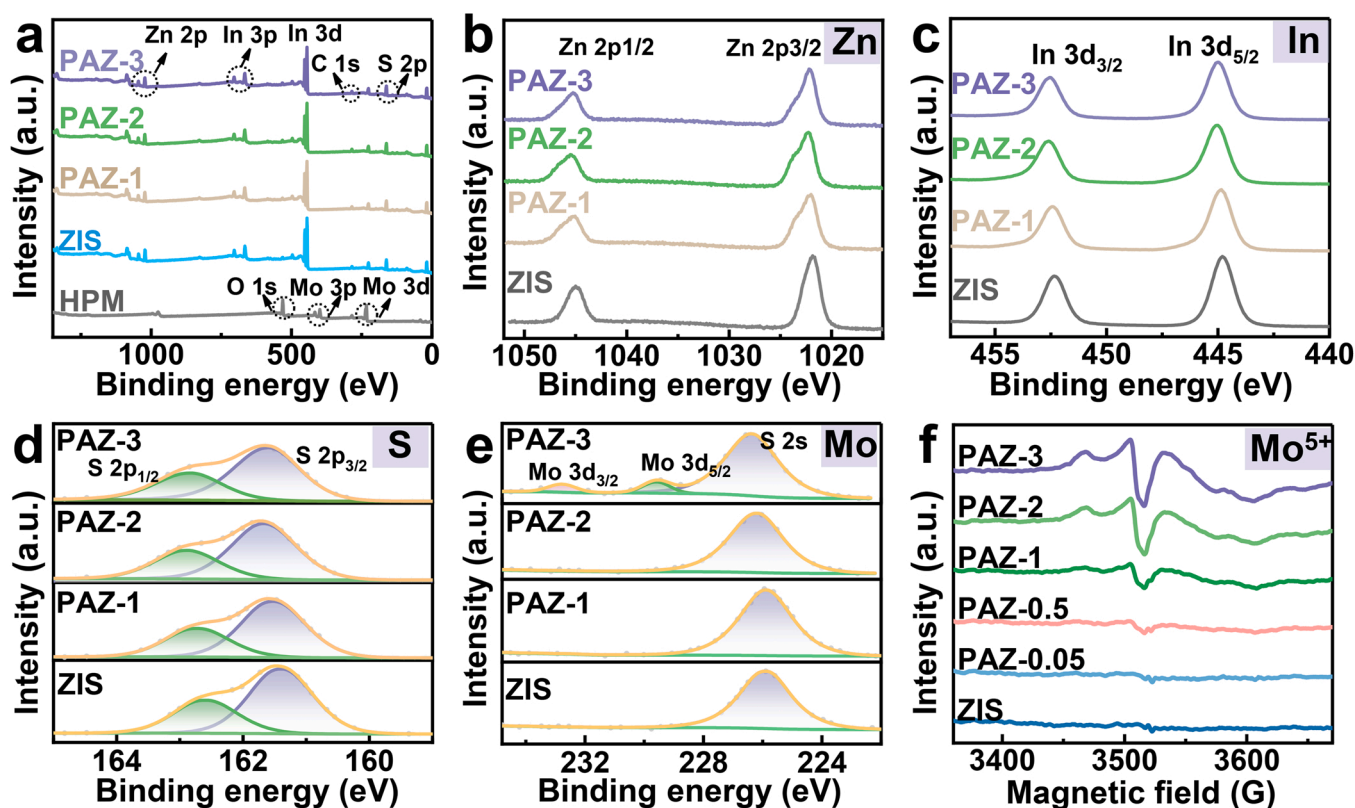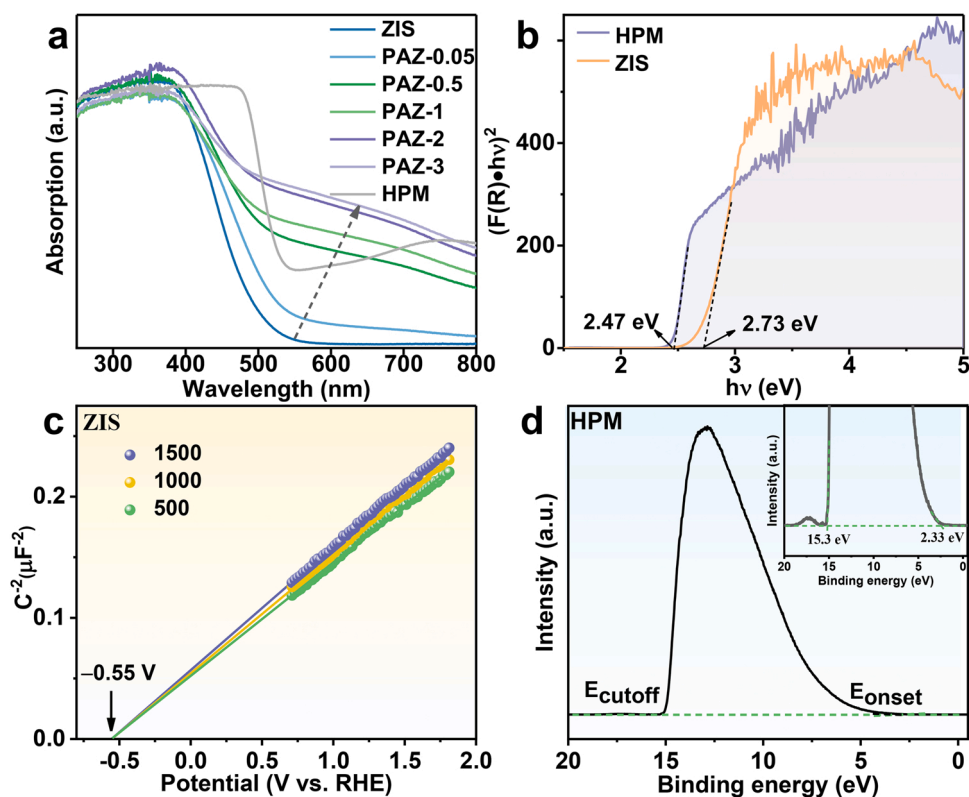

Fig. 3. (a) XPS survey spectra of ZIS, HPM, and PAZ-x (x = 1, 2, and 3). (b) Zn 2p, (c) In 3d, (d) S 2p, and (e) Mo 3d high-resolution spectra of ZIS and PAZ-x (x = 1, 2, and 3). (f) EPR tests for valence state analyses of Mo.

Fig. 4. (a) UV–Vis absorption spectra of ZIS, HPM, and PAZ-x (x = 0.05, 0.5, 1, 2, and 3). (b) Tauc plot of ZIS and HPM. (c) Mott–Schottky plot of ZIS. (d) UPS spectra of HPM.

of ZIS was measured to be −0.55 V (vs. RHE) as determined by Mott–Schottky plots (Fig. 4c). Since the flat potential of the n-semiconductor is very close to its conduction band (CB) potential, the CB potential of ZIS is estimated to be −0.55 V (vs. RHE). Therefore, the valence band (VB)

potential of ZIS is 2.18 V (vs. RHE). The HOMO level and work function (Φ) of HPM were calculated by ultraviolet photoemission spectroscopy (UPS) (Fig. 4d). The cutoff energy (E_{cutoff}) and onset energy (E_{onset}) are 15.3 and 2.33 eV, respectively. Based on the equation $\Phi = h\nu - E_{cutoff}$
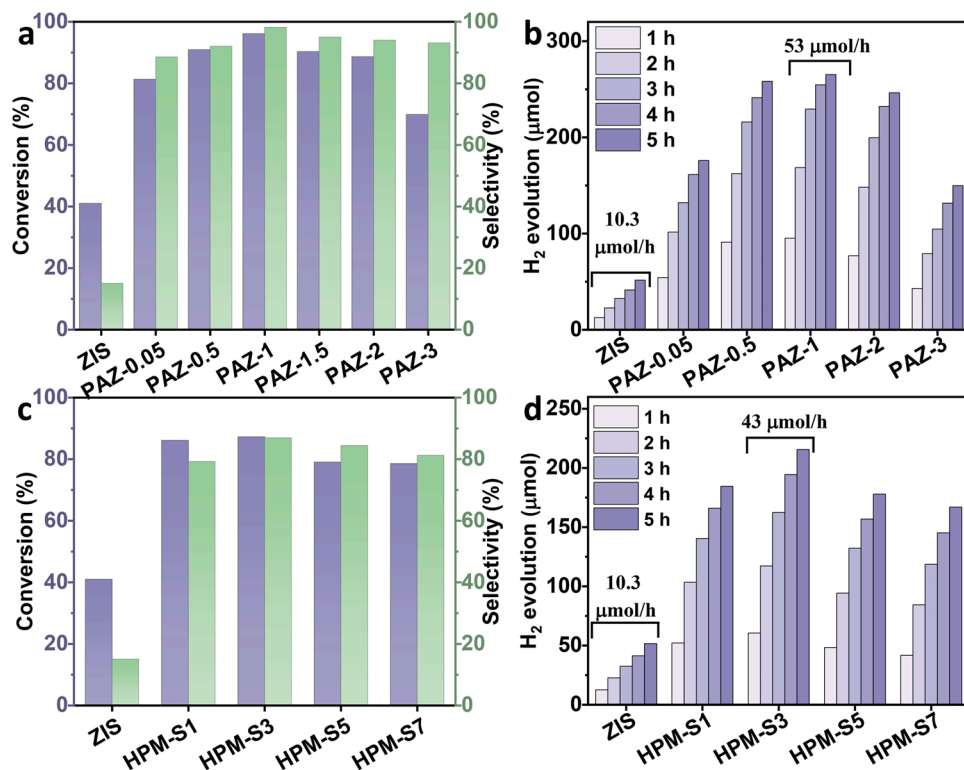
Fig. 5. Photocatalytic BA oxidation coupled with H_2 evolution: (a) BA conversion and BAD selectivity after 5 h irradiation for ZIS and PAZ-x samples, with (b) corresponding time-resolved H_2 production. (c) BA oxidation and (d) H_2-evolution performance for ZIS and HPM-SX samples (ZIS and HPM physical mixture; X represents the mass ratio of HPM to ZIS). Reaction conditions: 5 mg catalysts, 0.2 mmol BA, 10 mL deionized water, Ar atmosphere, visible light ($\lambda >$ 420 nm), 5 h, 25 °C.

($h\nu$ refers to the He I excitation energy of 21.22 eV), the work function of HPM is 5.92 eV (vs vacuum). Additionally, according to the equation $E_{VB} = E_{onset} + \Phi$ [48], the HOMO level of HPM was calculated to be 8.25 eV (vs. vacuum) or 3.81 V (vs. RHE) (E (vs. RHE) = E (vs. vacuum) − 4.44 eV). Hence, the LUMO level of HPM is 1.34 V (vs. RHE). The as-obtained band positions of ZIS and HPM are displayed in Fig. 6d.

3.3. Photocatalytic performance

The photocatalytic performance of BA conversion integrated with H_2 generation was investigated in a green aqueous medium instead of traditional organic solvents. The conversion of BA and the selectivity for benzaldehyde (BAD) after five hours catalyzed by ZIS and PAZ samples are presented in Fig. 5a. Moreover, the corresponding time-resolved H_2 production rate is displayed in Fig. 5b. The conversion and selectivity over pure ZIS are 41% and 15%, respectively, with the primary product being hydrobenzoin rather than BAD [49]. Pristine HPM clusters exhibit 9.58% conversion, and almost zero selectivity and H_2 production under the same reaction conditions. Although HPM possesses strong oxidation ability, its LUMO level is too low to reduce H^+, thus limiting the separation efficiency of charge carriers and impairing the oxidation process of BA. Comparatively, the photocatalytic activities over PAZ heterojunctions for oxidation of BA to BAD coupled with H_2 evolution are significantly improved compared with pure ZIS and HPM. Among the PAZ samples, PAZ-1 exhibited the highest photocatalytic activity, with BA conversion and BAD selectivity of up to 96.1% and 98.2%, respectively. The coupled H_2 production rate increases to 10.6 mmol·g^{-1}·h^{-1}, which is ca. five times higher than that of pure ZIS (2.06 mmol·g^{-1}·h^{-1}). Excitingly, when compared with previous reports on the photocatalytic oxidation of BA, our dual-functional HPM/ZIS photocatalytic system shows a remarkable photoredox advantage for both alcohol conversion and H_2 production even under an anaerobic atmosphere with water as the medium (Table S4). Therefore, the construction of HPM-incorporated ZIS heterojunctions plays an essential role in improving BA-to-BAD oxidation and proton reduction efficiency, which may benefit from faster photogenerated carrier transfer toward spatially separated surface locations promoted by the built-in electric field in PAZ heterojunctions. In addition, we tested time-resolved photocatalytic H_2 evolution in high-concentration BA aqueous solution (0.2 mol·L^{-1}) for ZIS and PAZ samples (Fig. S6). The linear increase in H_2 production is due to abundant electron donor sources. Moreover, the apparent quantum efficiency (AQE) for PAZ-1 at a wavelength of 420 nm reached 18.8% (Fig. S7). The dependence of AQE on light absorption suggests that the activities are induced by photocatalysis. For comparison, the performances over ZIS-HPM physical mixtures (HPM-SX, X represents the mass ratio of HPM to ZIS) were tested under the same conditions (Fig. 5c and d). Compared to pure ZIS, HPM-SX mixtures present an improved yield of BAD and H_2, which may be due to the presence of a built-in electric field as evidenced by color contrast experiments (Fig. S5). The time-dependent BA conversion over PAZ-1 and HPM-S3 samples was also tested (Fig. S8). After one hour, the BA conversion for the PAZ-1 and HPM-S3 samples reached 44.94% and 37.21%, respectively. Compared with the first hour, the conversion rate of BA gradually slowed down over the following four hours. This phenomenon could be ascribed to the gradual consumption of BA as irradiation time increased [50,51].

The stability of HPM/ZIS heterojunctions was demonstrated through multiple recycling tests. As displayed in Fig. S9, PAZ-1 shows negligible deterioration of photocatalytic activity after five consecutive cycles (25 h). The conversion and selectivity still reached 94.7% and 97.6%, respectively. The amount of H_2 production remained at 10.0 mmol·g^{-1}·h^{-1}. XPS tests (Fig. S10) further confirmed the unchanged element composition and electronic environment in recycled PAZ-1 compared to the pristine sample. Moreover, recycled PAZ-1 retained the hierarchical flower-like morphology assembled by ultrathin nanosheets (Fig. S11a). The XRD pattern (Fig. S11b) also

demonstrates the well-maintained crystal phase and crystallinity.

Other p-substituted benzyl alcohol substrates were also investigated over PAZ-1 (Fig. S12). Various substrates are efficiently converted to corresponding aldehydes coupled with H_2 evolution. In addition, there is an interesting electronic substituent effect on the photoconversion of aromatic alcohols. In comparison with BA, aromatic alcohols that are para-substituted with electron-donating groups –OCH$_3$ or –CH$_3$ exhibit slightly enhanced photocatalytic activities compared with those with electron-withdrawing groups –Cl or –Br. As reported, electron-donating groups could increase electron cloud density in benzene rings and thus promote the scission of C_α—H bonds in BA [52].

3.4. Mechanism of photogenerated charge carrier transfer

The separation and transfer of charge carriers are central issues closely related to photocatalytic activity. When semiconductors are in intimate contact, a built-in electric field drives the flow of photoinduced charge carriers at the interface [53]. To further demonstrate the impact of the built-in potential in PAZ heterojunctions on spatial separation of electron–hole pairs, we performed EPR and photoelectrochemical tests to reveal the charge transfer path and efficiency, respectively. As depicted in Fig. 6a, there is a detectable signal of DMPO–•OH radicals over HPM under illumination because the HOMO level of HPM (3.81 V vs. RHE) is more positive than the standard potential of H_2O/•OH radical (2.73 V vs. RHE) [54]. In contrast, we could not detect the signal of DMPO–•OH radicals over the ZIS sample because the VB potential of ZIS is 2.18 V (vs. RHE), which is in thermodynamically unfavorable for the oxidation of H_2O to •OH radical. Excitingly, a strong signal of DMPO–•OH radicals was observed for the PAZ-1 composites, illustrating that the photogenerated holes accumulate on the HOMO level of HPM rather than the VB of ZIS. The results fully confirm the Z-scheme charge transfer path in PAZ composites. Meanwhile, •O_2^- radical capture experiments were conducted to confirm the Z-scheme mechanism in the PAZ photocatalytic system (Fig. 6b). No DMPO–•O_2^- signal was observed on HPM because its LUMO level (1.34 V vs. RHE) is too low to reduce O_2 (0.08 V vs. RHE). The conduction band position (−0.55 V vs. RHE) of ZIS is higher than the standard potential of O_2/•O_2^- (0.08 V vs. RHE) [54], which favors the production of •O_2^- radicals. As expected, PAZ-1 shows a more robust DMPO–•O_2^- signal than pure ZIS, meaning that electrons are retained in the CB band of the ZIS component. Therefore, the built-in electric field in PAZ heterojunctions drives the recombination of the holes in the VB of ZIS and the electrons in the LUMO level of HPM/reduced-state HPM (HPB) under irradiation. The electrons left in the conduction band of ZIS and the holes in the HOMO level of HPM participate in H^+ ion reduction and BA oxidation, respectively (Fig. 6d).

More insights into the charge transfer efficiency following the Z-scheme path were obtained through photoelectrochemical experiments. As depicted in Fig. 7a, PAZ-1 exhibits a higher photocurrent intensity than ZIS and HPM, reflecting the promoted generation and separation of photoinduced charge carriers in PAZ heterojunctions. Interestingly, when turning off the light, the photocurrent of HPM exhibits slow decay rather than vanishing instantly. Thus, we conducted photocurrent decay tests over a long period to clearly present this phenomenon (Fig. 7b). After turning off the light source, the photocurrent over HPM attenuates exponentially over 250 s. Since there are multiple Mo^{6+} sites in the [PMo$_{12}$O$_{40}$]$^{3-}$ unit of HPM (inset in Fig. 1d), HPM could experience reversible multielectron transfer through valence state transformation in the metal centers (between Mo^{6+} and Mo^{4+}/Mo^{5+}) [24] (Fig. 3e and f). Therefore, HPM is known as "electron sponge" that stores and transmits electrons [5,46]. During the photocurrent test, HPM can store some photoinduced electrons in Mo sites and exists in a reduced state (HPB) [23]. The reduced-state HPM gradually returns to the ground state in the dark [55], resulting in an exponentially decaying photocurrent. In contrast, the photocurrent of PAZ-1 immediately vanishes when turning off the lamp, which proves the rapid consumption of photogenerated
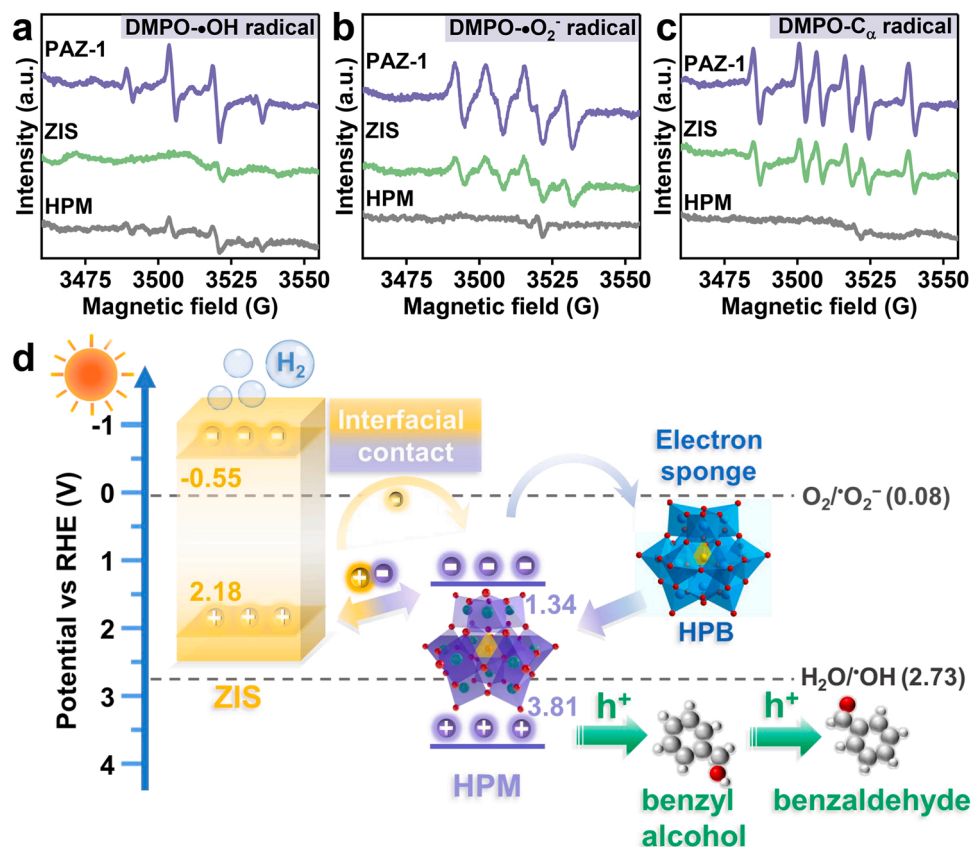
Fig. 6. EPR signals recorded for ZIS, HPM, and PAZ-1 in different systems under light irradiation ($\lambda > 420$ nm): (a) DMPO–$^{\bullet}$OH radical in pure water, (b) DMPO–$^{\bullet}$O$_2^-$ radical in methanol, and (c) DMPO–C$_\alpha$ radical in 0.02 M BA aqueous solution. (d) Schematic illustration of the Z-scheme transfer path of photogenerated carriers between HPM and ZIS heterojunctions. HPB refers to the reduction state of an HPM derived from the formation of a built-in electric field.
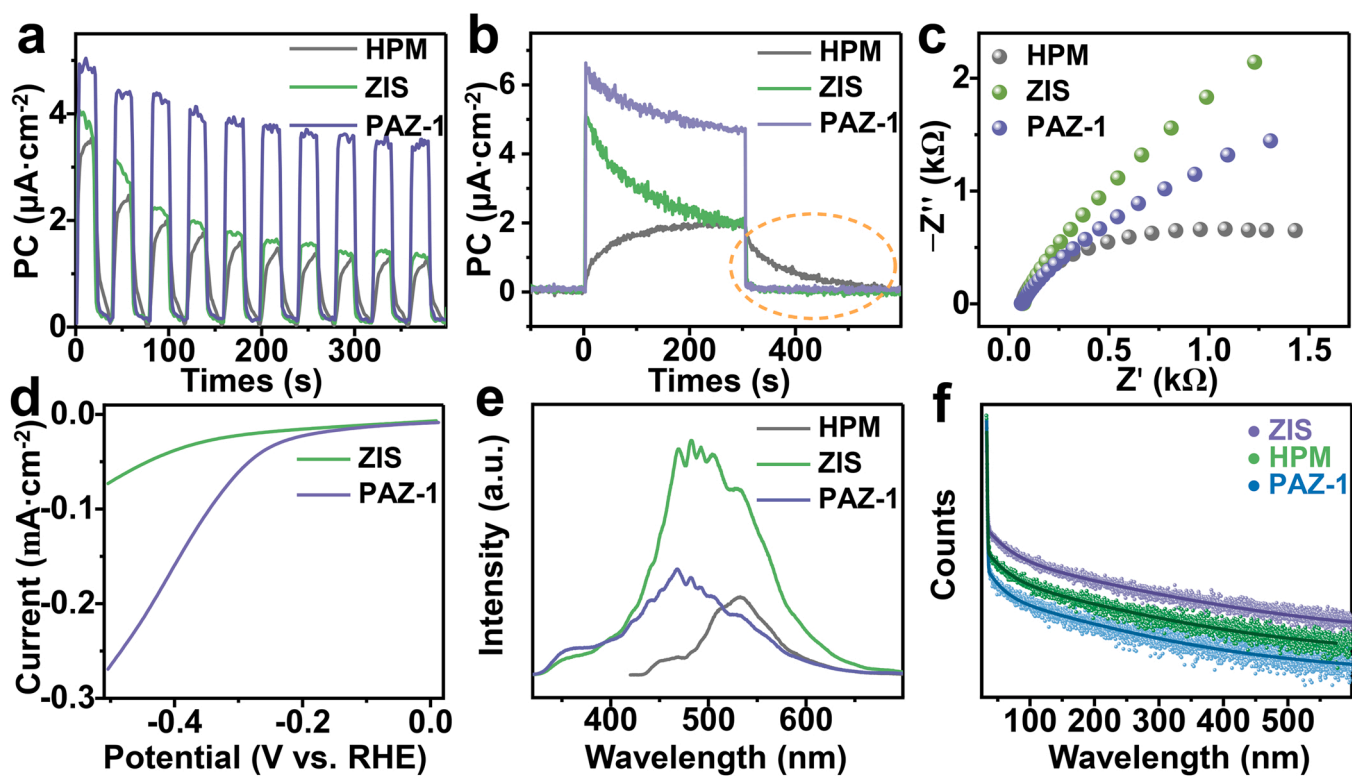

Fig. 7. (a) Periodic (on/off) photocurrent responses, (b) photocurrent decay, (c) EIS plots, (d) LSV curves for the HER, (e) steady-state PL spectra and (f) time-resolved PL decay of ZIS, HPM and PAZ-1.

electrons in HPM via recombination with photogenerated holes in ZIS. The above findings again confirm the Z-scheme mechanism. Additionally, a smaller semicircle of PAZ-1 than ZIS in the electrochemical impedance spectra (EIS) indicates a lower interfacial charge-transfer resistance, ensuring fast charge separation and transfer in PAZ heterojunctions (Fig. 7c). Pure HPM has a minor semicircle diameter due to its reversible redox properties [56]. Furthermore, the linear sweep voltammetry (LSV) (Fig. 7d) over PAZ-1 demonstrates its decreased overpotential, which favors faster H_2 release (Fig. 5b). Significant quenching of photoluminescence (PL) was observed after incorporating HPM into ZIS (Fig. 7e), illustrating the reduced recombination of charges. Moreover, the average fluorescent lifetimes of ZIS and HPM are 6.85 and 4.67 ns, respectively. In comparison, the average fluorescent lifetime is 2.41 ns for PAZ-1 (Fig. 7f, Table S2) owing to the fast transport of charge carriers due to Z-scheme heterojunctions.

3.5. Reaction mechanism

In addition to the transfer–separation efficiency of charge carriers, the consistency between photocatalytic activities and surface reaction kinetics drives us to explore possible BA oxidation processes. The adsorption of BA initiates the first step for the oxidation half-reaction. The zeta potentials of ZIS, HPM, and PAZ-1 are −31.1, −33.6, and −35.5 mV, respectively (Fig. S13). The more negative surface electricity of PAZ samples is favorable to BA adsorption due to the electrostatic interaction between the catalyst surface and alcohol hydroxyl groups [57]. The saturated adsorption capacity tests under dark conditions further verified a higher affinity of PAZ-1 to BA than pure ZIS (Fig. S14), which helps promote BA conversion. Next, a series of control experiments focused on the successive dehydrogenation oxidation process and main active species (Fig. S15) to discern the reaction mechanism. When employing carbon tetrachloride (CCl_4) as a quenching agent for photogenerated electrons, the conversion and selectivity for BA oxidation were almost unchanged. Nonetheless, the yield of H_2 dropped to almost zero, implying that photogenerated electrons participate in the formation of H_2 and have a negligible influence on the activation of BA. Triethanolamine (TEOA) and isopropanol (IPA) were used to distinguish the roles of holes and $^{\bullet}OH$ radicals in the conversion of BA. When TEOA was added to consume holes, the conversion of BA decreased to 28.1%, whereas H_2 production increased slightly. In addition, an inconspicuous conversion/selectivity/H_2 yield change was observed using IPA as a $^{\bullet}OH$ trapping agent. It can be concluded that the photogenerated holes drive the BA transformation, and the $^{\bullet}OH$ radical has little impact on the corresponding oxidation process. Furthermore, we found that the introduction of DMPO (radical scavenger) remarkably suppressed the conversion of BA (16.7%), meaning that the formation of BAD proceeds via radical intermediates. During the oxidation of BA, hydroxyl groups (–OH) and C_α—H bonds may be preferentially activated, producing corresponding oxygen-centered and carbon-centered radicals [18,56]. Diphenylamine (DPA), an oxygen-centered radical scavenger [58], was introduced to gain more insights into possible intermediate processes. The conversion was just 24.7% under this condition, illustrating that oxygen-centered radical intermediates play an important role in the photocatalytic oxidation of BA. We also conducted EPR tests using DMPO as a spin-trap reagent in 0.02 M BA solution to monitor other feasible reaction intermediate species (Fig. 6c). The characteristic sixfold peak signals reveal the generation of DMPO–C_α radical adducts during BA oxidation, resulting from the selective activation of the C_α—H bond of BA [59]. Notably, the signal intensity of DMPO–C_α radicals over PAZ-1 is higher than that of ZIS. Therefore, PAZ-1 produces more DMPO–C_α radicals than ZIS during the photocatalytic process, which is consistent with the activity results (Fig. 5a and b). Pure HPM showed no detectable DMPO–C_α radical signal for weak BA conversion performance. Isotope-labeling photocatalytic experiments were carried out to clarify the proton source of the produced hydrogen [60]. When D_2O is used instead of H_2O as the solvent, the main products are H_2 and HD,

accompanied by trace D_2 (Fig. S16). This result indicates that both benzyl alcohol and water can act as proton contributors. The lower quantities of HD and D_2 may be due to the heavier atomic mass of deuterium, which weakens its reactive activity [51]. To deeply understand the main proton source of H_2 and the adsorption priority of protons (from water or BA), pure MeCN was used as a solvent (Fig. S17). The H_2 yield and BA conversion are markedly lower in the MeCN system than in water. Thus, it is deduced that the protons from water preferentially adsorb to the catalyst surface and then accept electrons to contribute most of the H_2, which is in line with the results reported in the literature [51,61].

Based on the above results, we propose possible carbon-centered radical (I) and oxygen-centered radical (II) pathways for photocatalytic dehydrogenation oxidation of BA over PAZ heterojunctions (Scheme 1). Under visible irradiation, the photoexcited electrons and holes are localized in the ZIS and HPM, respectively, according to the Z-scheme transfer path driven by the built-in electric field. The catalysts with electronegative surfaces (Fig. S13) possess strong adhesion to the hydrogen of the –OH of BA and induce subsequent dehydrogenation steps. As a result, alkoxide anions ($PhCH_2O^-$) are formed [62], and the extractive protons from BA are adsorbed on the catalyst surface. The photoinduced holes in the HPM cluster can easily oxidize $PhCH_2O^-$ by attacking C_α—H bonds or O^- sites. When the former is preferentially attacked by holes, $PhCH_2O^-$ is activated to carbon-centered radicals via the cleavage of C_α—H (Path I), and the resulting protons are also adsorbed by catalysts. Next, the holes located at HPM continue to oxidize the obtained carbon-centered radical to produce BAD. In another pathway, the holes in HPM likely attack O^- sites in $PhCH_2O^-$, resulting in oxygen-centered radicals (Path II). Then the oxygen-centered radicals react with the photogenerated holes in HPM and undergo the dehydrogenation process to produce target products. Simultaneously, the protons extracted from BA or water are reduced by photogenerated electrons to yield H_2.

4. Conclusions

In summary, integrating the distinct oxidizing ability of POMs, we designed a dual-functional Z-scheme photocatalyst based on POM cluster-incorporated $ZnIn_2S_4$ nanosheets by secondary-component incorporation strategy. The driving force from built-in potential and intimate interfacial contact contribute to highly efficient interfacial charge transfer–separation during the photocatalytic process. By virtue of the synergy between POMs and ZIS, cooperative photoredox coupling of benzyl alcohol oxidation and H_2 evolution has been achieved under an anaerobic atmosphere using an aqueous medium without any organic solvents or oxidants. The conversion of BA is nearly 100%, and the simultaneous H_2-evolution rate reaches 10.6 mmol·g^{-1}·h^{-1}, which demonstrates a remarkable photoredox advantage for both alcohol conversion and H_2 production compared with recent reports (Table S4). From EPR and activity contrast experiments, we propose that the conversion of BA to BAD occurs through two kinds of transition states: carbon-centered radicals (I) and oxygen-centered radicals (II). This study represents the first application of POM-based materials for the cooperative coupling of anaerobic selective organic synthesis and H_2 production, which provides new inspiration for designing multifunctional POM-based photocatalytic systems for economic and ecological photoredox applications.

CRediT authorship contribution statement

Fangshu Xing: Conceptualization, Investigation, Validation, Formal analysis, Supervision, Writing – original draft. **Renyou Zeng:** Investigation, Validation, Formal analysis, Supervision. **ChuChu Cheng:** Validation, Formal analysis. **Qiuwen Liu:** Validation, Formal analysis. **Caijin Huang:** Conceptualization, Formal analysis, Supervision, Writing – review & editing.
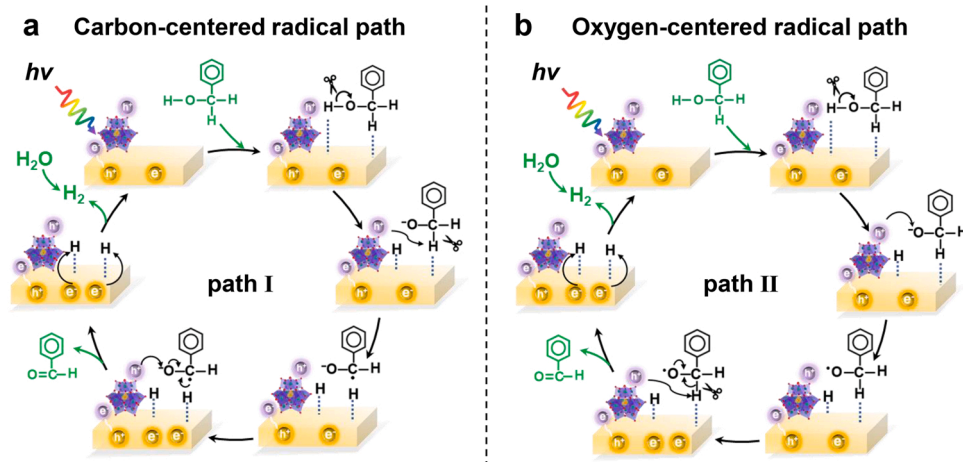
Scheme 1. Proposed reaction mechanism for selective photocatalytic BA oxidation coupled with H_2 evolution: (a) carbon-centered radical path and (b) oxygen-centered radical path.

Appendix A. Supporting information

Supplementary data associated with this article can be found in the online version at doi:10.1016/j.apcatb.2022.121087.

References

[1] Q. Li, Y. Ouyang, H. Li, L. Wang, J. Zeng, Photocatalytic conversion of methane: recent advancements and prospects, Angew. Chem. Int. Ed. 17 (2021), 2100428, https://doi.org/10.1002/anie.202108069.

[2] Z. Wang, C. Li, K. Domen, Recent developments in heterogeneous photocatalysts for solar-driven overall water splitting, Chem. Soc. Rev. 48 (2019) 2109–2125.

[3] Y. Zhao, G.I.N. Waterhouse, G. Chen, X. Xiong, L.Z. Wu, C.H. Tung, T. Zhang, Two-dimensional-related catalytic materials for solar-driven conversion of CO_x into valuable chemical feedstocks, Chem. Soc. Rev. 48 (2019) 1972–2010.

[4] Q. Wang, K. Domen, Particulate photocatalysts for light-driven water splitting: mechanisms, challenges, and design strategies, Chem. Rev. 120 (2020) 919–985.

[5] J. Xiao, X. Liu, L. Pan, C. Shi, X. Zhang, J.-J. Zou, Heterogeneous photocatalytic organic transformation reactions using conjugated polymers-based materials, ACS Catal. 10 (2020) 12256–12283.

[6] W.K. Shang, Y.G. Li, H.W. Huang, F.L. Lai, M.B.J. Roeffaers, B. Weng, Synergistic redox reaction for value-added organic transformation via dual-functional photocatalytic systems, ACS Catal. 11 (2021) 4613–4632.

[7] W.M. Cheng, R. Shang, Transition metal-catalyzed organic reactions under visible light: recent developments and future perspectives, ACS Catal. 10 (2020) 9170–9196.

[8] L. Xiong, J. Tang, Strategies and challenges on selectivity of photocatalytic oxidation of organic substances, Adv. Energy Mater. 11 (2021), 2003216.

[9] C. Bianchini, P.K. Shen, Palladium-based electrocatalysts for alcohol oxidation in half cells and in direct alcohol fuel cells, Chem. Rev. 109 (2009) 4183–4206.

[10] Z. Guo, B. Liu, Q. Zhang, W. Deng, Y. Wang, Y. Yang, Recent advances in heterogeneous selective oxidation catalysis for sustainable chemistry, Chem. Soc. Rev. 43 (2014) 3480–3524.

[11] R.H. Crabtree, Homogeneous transition metal catalysis of acceptorless dehydrogenative alcohol oxidation: applications in hydrogen storage and to heterocycle synthesis, Chem. Rev. 117 (2017) 9228–9246.

[12] C. Parmeggiani, C. Matassini, F. Cardona, A step forward towards sustainable aerobic alcohol oxidation: new and revised catalysts based on transition metals on solid supports, Gr. Chem. 19 (2017) 2030–2050.

[13] L. Chen, J. Tang, L.-N. Song, P. Chen, J. He, C.-T. Au, S.-F. Yin, Heterogeneous photocatalysis for selective oxidation of alcohols and hydrocarbons, Appl. Catal. B Environ. 242 (2019) 379–388.

[14] H. Li, F. Qin, Z. Yang, X. Cui, J. Wang, L. Zhang, New reaction pathway induced by plasmon for selective benzyl alcohol oxidation on BiOCl possessing oxygen vacancies, J. Am. Chem. Soc. 139 (2017) 3513–3521.

[15] Y. Dong, Y. Su, Y. Hu, H. Li, W. Xie, Ag_2S-CdS p-n nanojunction-enhanced photocatalytic oxidation of alcohols to aldehydes, Small 16 (2020), 2001529.

[16] S. Mazzanti, G. Manfredi, A.J. Barker, M. Antonietti, A. Savateev, P. Giusto, Carbon nitride thin films as all-in-one technology for photocatalysis, ACS Catal. 11 (2021) 11109–11116.

[17] Y.Z. Chen, Z.U. Wang, H. Wang, J. Lu, S.H. Yu, H.L. Jiang, Singlet oxygen-engaged selective photo-oxidation over Pt nanocrystals/porphyrinic MOF: the roles of photothermal effect and Pt electronic state, J. Am. Chem. Soc. 139 (2017) 2035–2044.

[18] M.Y. Qi, M. Conte, M. Anpo, Z.R. Tang, Y.J. Xu, Cooperative coupling of oxidative organic synthesis and hydrogen production over semiconductor-based photocatalysts, Chem. Rev. 121 (2021) 13051–13085, https://doi.org/10.1021/acs.chemrev.1c00197.

[19] B. Xia, Y. Zhang, B. Shi, J. Ran, K. Davey, S.Z. Qiao, Photocatalysts for hydrogen evolution coupled with production of value-added chemicals, Small Methods 4 (2020), 2000063.

[20] A.S. Cherevan, S.P. Nandan, I. Roger, R. Liu, C. Streb, D. Eder, Polyoxometalates on functional substrates: concepts, synergies, and future perspectives, Adv. Sci. 7 (2020), 1903511.

[21] L. Jiao, Y. Dong, X. Xin, R. Wang, H. Lv, Three-in-one: achieving a robust and effective hydrogen-evolving hybrid material by integrating polyoxometalate, a photo-responsive metal–organic framework, and in situ generated Pt nanoparticles, J. Mater. Chem. A 9 (2021) 19725–19733.

[22] S.S. Wang, G.Y. Yang, Recent advances in polyoxometalate-catalyzed reactions, Chem. Rev. 115 (2015) 4893–4962.

[23] I.A. Weinstock, R.E. Schreiber, R. Neumann, Dioxygen in polyoxometalate mediated reactions, Chem. Rev. 118 (2018) 2680–2717.

[24] K. Suzuki, N. Mizuno, K. Yamaguchi, Polyoxometalate photocatalysis for liquid-phase selective organic functional group transformations, ACS Catal. 8 (2018) 10809–10825.

[25] M. Zhang, X. Xin, Y. Feng, J. Zhang, H. Lv, G.-Y. Yang, Coupling Ni-substituted polyoxometalate catalysts with water-soluble CdSe quantum dots for ultraefficient photogeneration of hydrogen under visible light, Appl. Catal. B Environ. 303 (2022), 120893.

[26] N. Li, J. Liu, B.X. Dong, Y.Q. Lan, Polyoxometalate-based compounds for photo- and electrocatalytic applications, Angew. Chem. Int. Ed. 59 (2020) 20779–20793.

[27] L. Jiao, Y. Dong, X. Xin, L. Qin, H. Lv, Facile integration of Ni-substituted polyoxometalate catalysts into mesoporous light-responsive metal-organic framework for effective photogeneration of hydrogen, Appl. Catal. B Environ. 291 (2021), 120091.

[28] L.F. Wu, S. An, Y.F. Song, Heteropolyacids-immobilized graphitic carbon nitride: highly efficient photo-oxidation of benzyl alcohol in the aqueous phase, Engineering 7 (2021) 94–102.

[29] U. Caudillo-Flores, F. Ansari, B. Bachiller-Baeza, G. Colón, M. Fernández-García, A. Kubacka, $(NH_4)_4[NiMo_6O_{24}H_6]\cdot 5H_2O/g$-$C_3N_4$ materials for selective photo-oxidation of C-O and C=C bonds, Appl. Catal. B Environ. 278 (2020), 119299.

[30] J. Meng, X. Wang, X. Yang, A. Hu, Y. Guo, Y. Yang, Enhanced gas-phase photocatalytic removal of aromatics over direct Z-scheme-dictated $H_3PW_{12}O_{40}/g$-C_3N_4 film-coated optical fibers, Appl. Catal. B Environ. 251 (2019) 168–180.

[31] B. Yu, S. Zhang, X. Wang, Helical microporous nanorods assembled by polyoxometalate clusters for the photocatalytic oxidation of toluene, Angew. Chem. Int. Ed. 60 (2021) 17404–17409.

[32] M. Somekh, A.M. Khenkin, A. Herman, R. Neumann, Selective visible light aerobic photocatalytic oxygenation of alkanes to the corresponding carbonyl compounds, ACS Catal. 9 (2019) 8819–8824.

[33] V. Augugliaro, L. Palmisano, Green oxidation of alcohols to carbonyl compounds by heterogeneous photocatalysis, ChemSusChem 3 (2010) 1135–1138.

[34] T. Rüther, A.M. Bond, W.R. Jackson, Solar light induced photocatalytic oxidation of benzyl alcohol using heteropolyoxometalate catalysts of the type $[S_2M_{18}O_{62}]^{4-}$, Green Chem. 5 (2003) 364–366.

[35] J.Z. Liao, H.L. Zhang, S.S. Wang, J.P. Yong, X.Y. Wu, R. Yu, C.Z. Lu, Multifunctional radical-doped polyoxometalate-based host-guest material: photochromism and photocatalytic activity, Inorg. Chem. 54 (2015) 4345–4350.

[36] D. Li, X. Ma, Q. Wang, P. Ma, J. Niu, J. Wang, Copper-containing polyoxometalate-based metal-organic frameworks as highly efficient heterogeneous catalysts toward selective oxidation of alkylbenzenes, Inorg. Chem. 58 (2019) 15832–15840.

[37] X.H. Li, W.L. Chen, H.Q. Tan, F.R. Li, J.P. Li, Y.G. Li, E.B. Wang, Reduced state of the graphene oxide@polyoxometalate nanocatalyst achieving high-efficiency nitrogen fixation under light driving conditions, ACS Appl. Mater. Interfaces 11 (2019) 37927–37938.

[38] Y. Wang, H. Suzuki, J. Xie, O. Tomita, D.J. Martin, M. Higashi, D. Kong, R. Abe, J. Tang, Mimicking natural photosynthesis: solar to renewable H_2 fuel synthesis by Z-Scheme water splitting systems, Chem. Rev. 118 (2018) 5201–5241.

[39] Z. Li, C. Chen, E. Zhan, N. Ta, Y. Li, W. Shen, Crystal-phase control of molybdenum carbide nanobelts for dehydrogenation of benzyl alcohol, Chem. Commun. 50 (2014) 4469–4471.

[40] J.S. Li, X.J. Sang, W.L. Chen, L.C. Zhang, Z.M. Zhu, T.Y. Ma, Z.M. Su, E.B. Wang, Enhanced visible photovoltaic response of TiO_2 thin film with an all-Inorganic donor-acceptor type polyoxometalate, ACS Appl. Mater. Interfaces 7 (2015) 13714–13721.

[41] Y. Pan, X. Yuan, L. Jiang, H. Yu, J. Zhang, H. Wang, R. Guan, G. Zeng, Recent advances in synthesis, modification and photocatalytic applications of micro/nano-structured zinc indium sulfide, Chem. Eng. J. 354 (2018) 407–431.

[42] F. Xing, Q. Liu, C. Huang, Mo-doped $ZnIn_2S_4$ flower-like hollow microspheres for improved visible light-driven hydrogen evolution, Sol. RRL 4 (2019), 1900483.

[43] F.S. Xing, C.C. Cheng, J.W. Zhang, Q.W. Liu, C. Chen, C.J. Huang, Tunable charge transfer efficiency in $H_xMoO_3@ZnIn_2S_4$ hierarchical direct Z-scheme heterojunction toward efficient visible-light-driven hydrogen evolution, Appl. Catal. B Environ. 285 (2021), 119818.

[44] D. Yang, S. Zuo, H. Yang, X. Wang, Single-unit-cell catalysis of CO_2 electroreduction over sub-1 nm Cu_9S_5 Nanowires, Adv. Energy Mater. 11 (2021), 2100272.

[45] P. Wang, Z. Shen, Y. Xia, H. Wang, L. Zheng, W. Xi, S. Zhan, Atomic insights for optimum and excess doping in photocatalysis: a case study of few-Layer Cu-$ZnIn_2S_4$, Adv. Funct. Mater. 29 (2019), 1807013.

[46] H. Wang, S. Hamanaka, Y. Nishimoto, S. Irle, T. Yokoyama, H. Yoshikawa, K. Awaga, In operando X-ray absorption fine structure studies of polyoxometalate molecular cluster batteries: polyoxometalates as electron sponges, J. Am. Chem. Soc. 134 (2012) 4918–4924.

[47] W. Liu, W. Mu, M. Liu, X. Zhang, H. Cai, Y. Deng, Solar-induced direct biomass-to-electricity hybrid fuel cell using polyoxometalates as photocatalyst and charge carrier, Nat. Commun. 5 (2014) 3208.

[48] J. Hu, C. Chen, Y. Zheng, G. Zhang, C. Guo, C.M. Li, Spatially separating redox centers on Z-Scheme $ZnIn_2S_4/BiVO_4$ hierarchical heterostructure for highly efficient photocatalytic hydrogen evolution, Small 16 (2020), 2002988.

[49] Q. Lin, Y.-H. Li, M.-Y. Qi, J.-Y. Li, Z.-R. Tang, M. Anpo, Y.M.A. Yamada, Y.-J. Xu, Photoredox dual reaction for selective alcohol oxidation and hydrogen evolution over nickel surface-modified $ZnIn_2S_4$, Appl. Catal. B Environ. 271 (2020), 118946.

[50] A. Mahdavi-Shakib, J. Sempel, L. Babb, A. Oza, M. Hoffman, T.N. Whittaker, B. D. Chandler, R.N. Austin, Combining benzyl alcohol oxidation saturation kinetics and hammett studies as mechanistic tools for examining supported metal catalysts, ACS Catal. 10 (2020) 10207–10215.

[51] B. Wu, L. Zhang, B. Jiang, Q. Li, C. Tian, Y. Xie, W. Li, H. Fu, Ultrathin porous carbon nitride bundles with an adjustable energy band structure toward simultaneous solar photocatalytic water splitting and selective phenylcarbinol oxidation, Angew. Chem. Int. Ed. 60 (2021) 4815–4822.

[52] N.Y. Oh, Y. Suh, M.J. Park, M.S. Seo, J. Kim, W. Nam, Mechanistic insight into alcohol oxidation by high-valent iron-oxo complexes of heme and nonheme ligands, Angew. Chem. 117 (2005) 4307–4311.

[53] X. Liu, Q. Zhang, D. Ma, Advances in 2D/2D Z-scheme heterojunctions for photocatalytic applications, Sol. RRL 5 (2020), 2000397.

[54] P.M. Wood, The potential diagram for oxygen at pH 7, Biochem. J. 253 (1988) 287–289.

[55] M. Yoon, J.A. Chang, Y. Kim, J.R. Choi, K. Kim, S.J. Lee, Heteropoly acid-incorporated TiO_2 colloids as novel photocatalytic systems resembling the photosynthetic reaction center, J. Phys. Chem. B 105 (2001) 2539–2545.

[56] L. Yang, J. Lei, J.M. Fan, R.M. Yuan, M.S. Zheng, J.J. Chen, Q.F. Dong, The intrinsic charge carrier behaviors and applications of polyoxometalate clusters based materials, Adv. Mater. 33 (2021) 2005019.

[57] H. Hao, L. Zhang, W. Wang, S. Qiao, X. Liu, Photocatalytic hydrogen evolution coupled with efficient selective benzaldehyde production from benzyl alcohol aqueous solution over $ZnS-Ni_xS_y$ composites, ACS Sustain. Chem. Eng 7 (2019) 10501–10508.

[58] Z. Li, J. Zhang, X. Jing, J. Dong, H. Liu, H. Lv, Y. Chi, C. Hu, A polyoxometalate@ covalent triazine framework as a robust electrocatalyst for selective benzyl alcohol oxidation coupled with hydrogen production, J. Mater. Chem. A 9 (2021) 6152–6159.

[59] S. Meng, X. Ye, J. Zhang, X. Fu, S. Chen, Effective use of photogenerated electrons and holes in a system: photocatalytic selective oxidation of aromatic alcohols to aldehydes and hydrogen production, J. Catal. 367 (2018) 159–170.

[60] M. Liu, L.-Z. Qiao, B.-B. Dong, S. Guo, S. Yao, C. Li, Z.-M. Zhang, T.-B. Lu, Photocatalytic coproduction of H_2 and industrial chemical over MOF-derived direct Z-scheme heterostructure, Appl. Catal. B Environ. 273 (2020), 119066.

[61] L. Jiao, D. Zhang, Z. Hao, F. Yu, X.-J. Lv, Modulating the energy band to inhibit the over-oxidation for highly selective anisaldehyde production coupled with robust H_2 evolution from water splitting, ACS Catal. 11 (2021) 8727–8735.

[62] Z. Chai, T.T. Zeng, Q. Li, L.Q. Lu, W.J. Xiao, D. Xu, Efficient visible light-driven splitting of alcohols into hydrogen and corresponding carbonyl compounds over a Ni-modified CdS photocatalyst, J. Am. Chem. Soc. 138 (2016) 10128–10131.